Applied Physics Letters

Terahertz solid immersion microscopy: Recent achievements and challenges

Cite as: Appl. Phys. Lett. **120**, 110501 (2022); https://doi.org/10.1063/5.0085906
Submitted: 20 January 2022 • Accepted: 04 March 2022 • Published Online: 14 March 2022

N. V. Chernomyrdin, M. Skorobogatiy, D. S. Ponomarev, et al.

Terahertz solid immersion microscopy: Recent achievements and challenges

Cite as: Appl. Phys. Lett. **120**, 110501 (2022); doi: 10.1063/5.0085906
Submitted: 20 January 2022 · Accepted: 4 March 2022 ·
Published Online: 14 March 2022

View Online Export Citation CrossMark

N. V. Chernomyrdin,[1,2] M. Skorobogatiy,[3] D. S. Ponomarev,[4] V. V. Bukin,[1] V. V. Tuchin,[5,6] and K. I. Zaytsev[1,2,a)]

AFFILIATIONS

[1]Prokhorov General Physics Institute of the Russian Academy of Sciences, Moscow, Russia
[2]Bauman Moscow State Technical University, Moscow, Russia
[3]Department of Engineering Physics, Polytechnique Montreal, Montreal, Quebec H3C 3A7, Canada
[4]V.G. Mokerov Institute of Ultra High Frequency Semiconductor Electronics of the Russian Academy of Sciences, Moscow, Russia
[5]Science Medical Center, Saratov State University, Saratov, Russia
[6]Institute of Precision Mechanics and Control, FRC "Saratov Scientific Centre of the Russian Academy of Sciences," Saratov, Russia

[a)]Author to whom correspondence should be addressed: kirzay@gmail.com

ABSTRACT

Unique effects of terahertz (THz)-wave–matter interaction push rapid progress in THz optoelectronics aimed at bridging the problematic THz gap. However, majority of modern methods of THz spectroscopy and imaging are still hampered by low spatial resolution. Common lens/mirror-based THz optics fails to overcome the Abbe barrier and usually provides resolution larger than a free-space wavelength λ (i.e., hundreds of micrometers or even few millimeters). To mitigate this difficulty, supperresolution THz imaging modalities were introduced recently, among which we particularly underline different methods of THz scanning-probe near-field microscopy. They not only rely on strong light confinement on sub-wavelength probes and provide resolution down to $\sim 10^{-1}$–$10^{-3}\lambda$ but also suffer from small energy efficiency or presume an interplay among imaging resolution, signal-to-noise ratio, and performance. In this paper, we consider reflection-mode THz solid immersion (SI) microscopy that offers some compromise between the high imaging resolution of 0.15λ and high energy efficiency, which is due to the absence of any subwavelength probe in an optical scheme. Recent achievements, challenging problems, and prospects of SI microscopy are overviewed with an emphasis on resolving the inverse problem and applications in THz biophotonics.

THz technology is rapidly developed nowadays,[1–5] which is driven by the unique features of THz-wave–matter interactions[6] and prospects of THz tools in different branches of science and technology such as astrophysics,[7,8] condensed matter physics and materials science,[9,10] chemistry and pharmaceutical industry,[11] food science,[12] nondestructive testing,[13] beyond 5G communications,[14] medical diagnosis,[15,16] and therapy.[17]

The aforementioned applications of THz technology suffer from low spatial resolution of commonly used THz optical systems.[2,6,15] They usually utilize lens- or mirror-based optics, the resolution of which obeys the $\simeq 0.5\lambda$ Abbe diffraction limit of free-space focusing. Due to large THz wavelengths, resolution of such systems appears at the scale of few hundreds of micrometers or even few millimeters, even for a wide-aperture optics.[18] Overcoming this barrier is of particular importance in THz biophotonics,[6,15,17] where the limited resolution does not allow to study subwavelength tissue heterogeneties, detect small-scale neoplasms, accurately delineate the tumor margins, and locally expose tissues to THz waves. Moreover, it limits the dimensions of defects, which can be detected during THz nondestructive testing, or the diversity of materials, which can be studied in the THz range.

To address this challenge, recently, numerous approaches to improve the spatial resolution of THz spectroscopy and imaging have been proposed.[2,6,15] First, we consider modern methods of image reconstruction, which form an inexpensive approach to boost the performance of almost any THz imaging system. They rely on modeling of the imaging system point spread function followed by the image reconstruction via the deconvolution or inverse filtering.[19] The resultant resolution enhancement is on the order of tens of percent, but it still obeys the Abbe limit. Another option is based on THz digital holography, synthetic aperture, and computational imaging,[20–22] which are capable of slightly sub-wavelength resolution, but still cannot overcome the Abbe diffraction limit. They also require complicated techniques to resolve the inverse problems and are accompanied by unique image noises and distortions that somewhat limits their practical utility.

Other prospective modalities of superresolution THz imaging rely on the photonic jet phenomenon.[23–25] The term "photonic jet" describes electromagnetic beam confinement at the shadow side of a mesoscale dielectric particle illuminated by a plane or slightly convergent wave with the resultant lateral dimensions of beam caustic as small as $\sim 10^{-1}\lambda$. This effect allows us to boost the resolution of almost any THz focusing system by simply placing a judiciously designed dielectric particle in front of the focal plane.[24] At the same time, problems of a dielectric particle handling near the focal plane and its moving over the object surface somewhat limit practical utility of this principle.

Then, one can consider different methods of THz scanning-probe near-field optical microscopy (SNOM) that can be classified into the tip- and aperture-based ones. The tip-based SNOM detects the THz field scattered by a metal or dielectric cantilever, which is placed in close proximity to an object with the resultant resolution down to $10^{-2}\lambda$–$10^{-4}\lambda$.[26,27] Particularly, such an advanced resolution allows one to map the THz conductivity in semiconductor materials and devices.[28,29] We should note several exotic THz imaging modalities, which are based on a tapered Sommerfeld wire[30] and a wire medium,[31,32] providing the resolution of $\geq 10^{-1}\lambda$ due to plasmonic mode confinement on a metal wire. One should also emphasize a flexible sapphire fiber[33] and a sapphire fiber bundle[34] allowing the resolution of ≥ 2–$5\times 10^{-1}\lambda$, thanks to a guided mode confinement in a solid core of a high-refractive-index fiber that can also be attributed to the discussed above tip-based SNOM.

In turn, the aperture-based SNOM uses subwavelength diaphragms to either illuminate an object or collect the scattered THz field at its shadow side, while their resolution is mainly determined by the aperture dimensions that can be as small as $\sim 10^{-1}$–$10^{-2}\lambda$.[35–37] Despite the beneficial resolution, all SNOM systems suffer from a low optical throughout due to the use of subwavelength tips and apertures in an optical scheme. Therefore, to achieve appropriate image quality, SNOM generally requires powerful emitters, sensitive detectors, and long image acquisition times. This difficulty can be partially mitigated using innovative coded-aperture near-field THz microscopy[38] or laser scanning-point THz source microscopy.[39,40] Nevertheless, all SNOM techniques require a very small working distance between the scanning probe and an imaged objects; thus, the probe may interact with an object and even perturb its structure and distort the THz image. SNOM systems have limited capabilities in imaging of amorphous media and soft biological tissues, which considerably limit their utility in THz biophotonics and medical imaging. Thereby, the discussed SNOM systems are still remain the laboratory research tools.

In this review, we focus on SI microscopy, which was first introduced in 1990 to achieve subwavelength resolution in the visible (VIS) and infrared (IR) ranges[41] and recently transferred to the millimeter-wave and THz ranges.[42–44] The essence of the SI effect is a reduction in the electromagnetic-beam caustic (focal spot) dimensions, when the beam is focused in free space at a small distance ($\ll \lambda$) behind the high-refractive-index optical element (i.e., the so-called SI lens) with a contribution of evanescence waves of the total internal reflection (TIR).[45] Typically, the SI optical system consists of two parts:

- the basic wide-aperture lens that provides high spatial resolution itself but still obeys the diffraction barrier, and.
- the high-refractive-index SI lens that is placed in front of the imaging plane and serves as a resolution enhancer.

Figure 1 shows the common reflection-mode hemispherical SI lens, which is radiated from the top side by a focused electromagnetic wave formed by a basic wide-aperture lens. The spherical surface of the SI lens is concentric for the converging wavefront in order to avoid refraction and related chromatic aberrations, while its flat surface coincidences with the object plane. Here, n_{SI} and n_{obj} stand for the refractive indices of the SI lens material and an imaged object, respectively. A spherical electromagnetic wave enters the SI lens and then is reflected at the SI lens–object (free space) interface and divided into two parts. For incidence angles θ below the critical TIR angle $\theta < \theta_{TIR} = \arcsin(n_{obj}/n_{SI})$, the ordinary reflection occurs, while for higher angles $\theta \geq \theta_{TIR}$, the TIR effect takes place, and the evanescent waves are excited at the analyzed interface. Both ordinary and evanescent waves contribute to formation of the subwavelength beam caustic, which exists at the shadow side of this interface.

The resolution enhancement through a SI lens can be explained by a reduction in the electromagnetic wavelength near the analyzed interface (as compared to a free-space wavelength λ) for both ordinary-reflected and evanescent waves. Indeed, the ordinary wave travels inside the high-refractive-index SI lens material and, thus, has the wavevector $\mathbf{k}_{ord}$ and wavelength λ_{ord} of

$$\mathbf{k}_{ord} = \mathbf{k} n_{SI}, \quad \lambda_{ord} = \frac{\lambda}{n_{SI}}, \tag{1}$$

where $\mathbf{k}$ is a free-space wavevector. Here, λ_{ord} is n_{SI}-times smaller than λ. The evanescent wave propagates along the SI lens–object interface[54] and has the wavevector $\mathbf{k}_{evan}$ and the effective wavelength λ_{evan} of

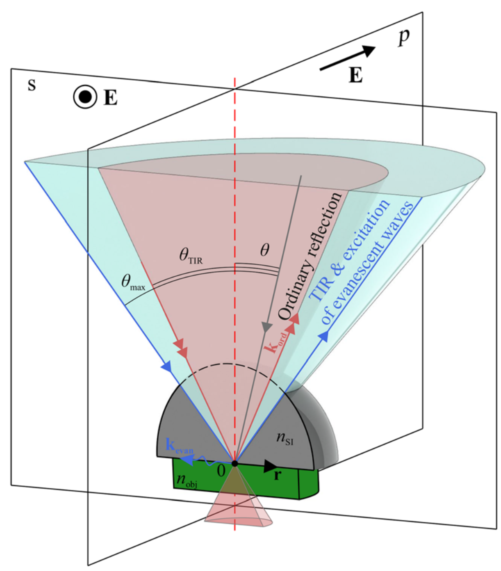

FIG. 1. Schematic of the reflection-mode SI lens based on a high-refractive-index hemisphere. Here, a basic wide-aperture lens that forms a convergent wavefront is not shown for simplicity.

$$\mathbf{k}_{\mathrm{evan}} = \mathbf{k} n_{\mathrm{SI}} \sin(\theta), \quad \lambda_{\mathrm{evan}} = \frac{\lambda}{n_{\mathrm{SI}} \sin(\theta)}. \tag{2}$$

Here, λ_{evan} is also reduced by a factor of $n_{\mathrm{SI}} \sin(\theta)$ or $\sim n_{\mathrm{SI}}$ at high angles θ. Such a wavelength reduction underlies the common $\simeq n_{\mathrm{SI}}$-times reduction in the focal spot dimensions provided by most SI lenses. Standard analytical approaches of geometrical optics and scalar diffraction theory[54,55] fail to describe all peculiarities of beam focusing by a SI lens, such as the exact focal spot geometry, system resolution, and depth of fields. This is due to a wide beam aperture and a near-field operation regime of such systems. To analyze the details of SI lens performance, methods of computational electrodynamics are usually used, which allow one to take into account such effects as interplay among ordinary and evanescent waves, electromagnetic beam polarization, apodization, and aberrations.[49,56–62]

Since its discovery, the SI optics was vigorously explored and transferred to other spectral ranges and found a variety of applications. As it is highlighted in Fig. 2, different SI lens arrangements were studied to meet the demands of supperresolution imaging and exposure in the VIS and IR ranges. Figure 2(a) shows a hyperhemispherical super-SI lens with radius R and height $h \simeq R(1 + 1/n_{\mathrm{SI}})$. Thanks to the additional electromagnetic-wave refraction at the spherical surface of a lens, the resolution enhancement can reach $\sim n_{\mathrm{SI}}^2$, but such a lens suffers from material dispersion and chromatic aberration.[46,63] In Figs. 2(b) and 2(c), concepts of the diffractive[47] and annular-aperture SI lenses[48,49] are illustrated. They are aimed at reducing the SI lens dimensions, improving its resolution or field of view. As a particular example of the annular-aperture SI lens, in Ref. 64, the angles θ above the critical TIR one θ_{TIR} were selected, while the ordinary beam part was blocked. This allows excitation of only the evanescent waves, thus, localizing the beam caustic in the axial direction. Figures 2(d) and 2(e) show two distinct microfabricated SI lenses, developed for the IR (9.5 μm)[50] and VIS[51] ranges. In Figs. 2(f) and 2(g), a planar VIS SI parabolic mirror coupled to a planar waveguide is shown along with a resultant light intensity distribution formed by such an element at 413 nm and measured via SNOM.[52] Finally, in Figs. 2(h)–2(j), we show a metamaterial-based VIS SI lens made of the self-assembled TiO_2 nanoparticles and superresolution images collected by this system.[53]

From Fig. 3, we notice that SI optics found a number of applications in different branches of science and technology. First, we consider applications of the SI lens in lithography.[65,72] For example, Fig. 3(a) shows an atomic force microscopy image of lines in a photoresist (Shipley SPR 3001) on a silicon wafer that is formed by VIS (442 nm) SI photolithography and possesses the subwavelength width and depth of $\simeq$ 190 and 50 nm.[65] SI microscopy was applied for thermal imaging,[66,73] including the studies of heat dissipation in electrical circuits. For example, Fig. 3(b) shows the modulated thermal image of a gold resistor dissipating 609 mW power that is collected through a 500-μm-thick silicon substrate via a 440-nm-resolution near-IR (1.0–1.7 μm) SI lens.[66] Moreover, SI optics is considered as a prospective tool for optical data storage.[67,74–76] As an example, in Fig. 3(c), we show the VIS SNOM image of marks in a phase-change sample formed on a glass substrate by a 5 nm-thick $ZnS\text{-}SiO_2$ dielectric layer, a 20-nm-thick $Ge_2Sb_2Te_5$ phase-change layer, and a 120-nm-thick $ZnS\text{-}SiO_2$ dielectric layer.[67] These marks were written using a near-IR (0.83 μm) parabolic

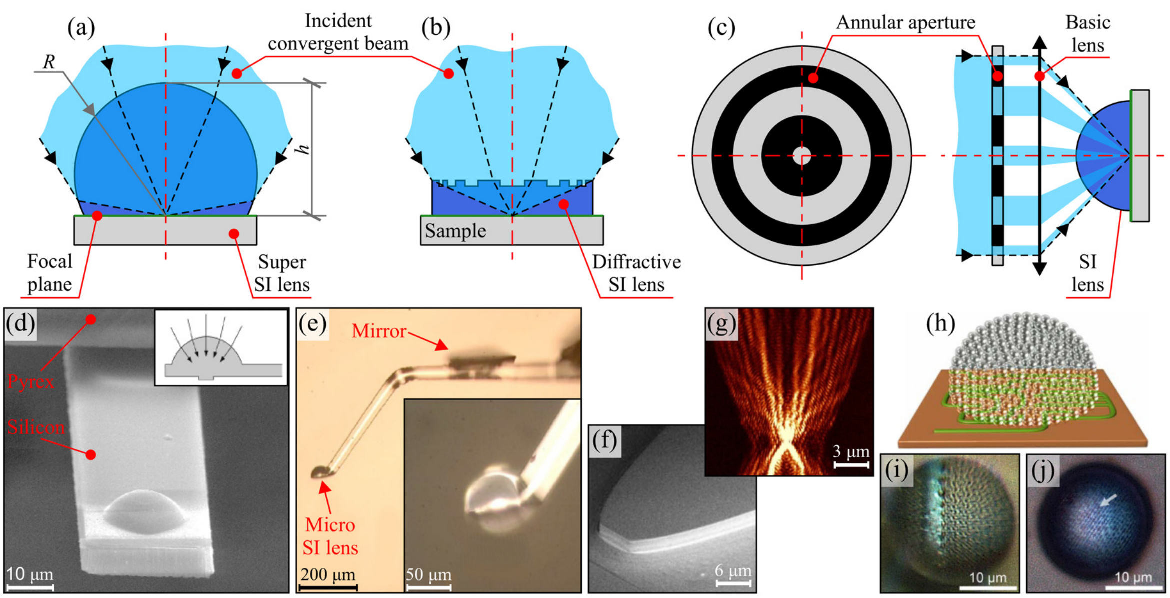

FIG. 2. Different SI lens arrangements. (a)–(c) Schematics of the super-SI (or Weierstrass),[46] diffractive,[47] and annular-aperture[48,49] SI lenses. (d) and (e) Microscopy of the microfabricated middle-IR and VIS SI lenses. Panels (d) and (c) are reproduced with the permission from Fletcher *et al.*, Appl. Phys. Lett. **77**, 2109–2111 (2000). Copyright 2000 AIP Publishing; and Lerman *et al.*, Appl. Phys. Lett. **89**, 223122 (2006). Copyright 2006 AIP Publishing, respectively. (f) Microscopy of the planar VIS SI parabolic mirror coupled to a planar waveguide and (g) measured light intensity distribution. Panels (f) and (g) are reproduced with the permission from Challener *et al.*, Opt. Express **13**, 7189–7197 (2005). Copyright 2005 The Optical Society. (h) Schematic of the metamaterial-based VIS SI lens and its applications for imaging of (i) a nanopatterned wafer and (j) a blue-ray disk. Panels (h)–(j) are reproduced with permission from Fan *et al.*, Sci. Adv. **2**, 40–42 (2016). Copyright 2016 Authors, licensed under a Creative Commons Attribution (CC BY) license.

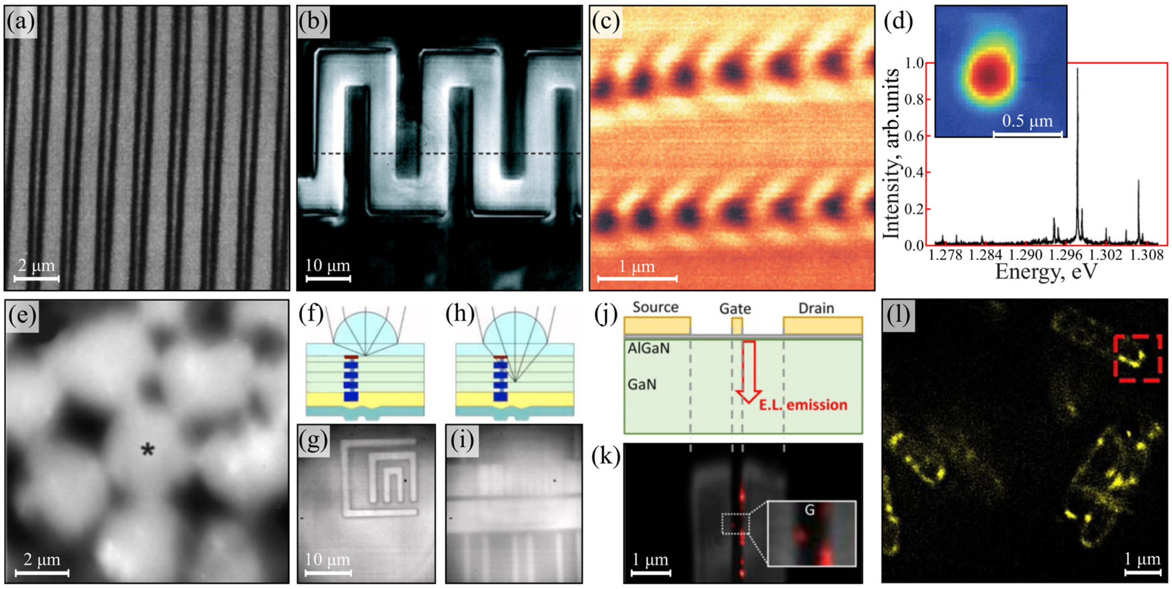

FIG. 3. Applications of SI optics in the VIS and near-IR ranges. (a) Photoresist film patterned by SI-lens-based photolithography. Panel (a) is reproduced with permission from Ghislain *et al.*, Appl. Phys. Lett. **74**, 501–503 (1999). Copyright 1999 AIP Publishing. (b) Near-IR SI imaging of a gold resistor dissipating heat. Panel (b) is reproduced with permission from Tessier *et al.*, Appl. Phys. Lett. **90**, 171112 (2007). Copyright 2007 AIP Publishing. (c) Marks in a phase-change coating written by a near-IR parabolic SI mirror. Panel (c) is reproduced with permission from Peng *et al.*, Appl. Phys. Lett. **87**, 151105 (2005). Copyright 2005 AIP Publishing. (d) Photoluminescence near-IR SI spectroscopy and imaging of a single quantum dot. Panel (d) is reproduced with permission from Liu *et al.*, Appl. Phys. Lett. **87**, 071905 (2005). Copyright 2005 AIP Publishing. (e) Raman SI image of a micropatterned transparent organic conductor film. Panel (e) is reproduced with permission from C. Michaels, J. Raman Spectrosc. **41**, 1670–1677 (2010). Copyright 2010 John Wiley & Sons. (f)–(i) Subsurface near-IR SI microscopy of a multilayer integrated circuit. Panels (f)–(i) are reproduced with permission from Koklu *et al.*, Opt. Express **16**, 9501 (2008). Copyright 2008 The Optical Society. (j) and (k) Electroluminescence emission VIS SI microscopy of a degraded AlGaN/GaN transistor. Panels (j) and (k) are reproduced with permission from J. Pomeroy and M. Kuball, J. Appl. Phys. **118**, 144501 (2015). Copyright 2015 AIP Publishing. (l) Fluorescence cryogenic super-SI microscopy of *E. coli* cells. Panel (l) is reproduced with permission from Wang *et al.*, Commun. Biol. **2**, 74 (2019). Copyright 2019 Authors, licensed under a Creative Commons Attribution (CC BY) license.

SI mirror [similar to that from Fig. 2(f)], while the distance between the neighboring marks is slightly subwavelength $\simeq 0.5\,\mu$m. In Fig. 3(d), we show the results of near-IR SI measurements of the photoluminescence spectrum and the image of an individual InGaAs/GaAs quantum dot.[68] The data were collected with the spatial resolution of 350 nm, while the excitation laser energy and the sample temperature were 1.476 eV and 8 K, respectively.

Moreover, SI microscopy was applied for studying the Raman effect in dielectrics and semiconductors.[51,69,77] In Fig. 3(e), the SI Raman image of a micropatterned transparent organic conductor film placed on a polyethylene terephthalate substrate is shown.[69] A 785 nm diode laser was used to excite the sample, while the resultant image represents a 440 cm^{-1} peak area in the observed Raman spectrum. Among the most promising applications of SI microscopy, we should notice nondestructive testing of semiconductor devices and electrical circuits.[64,68,70,71,78–80] In Figs. 3(f)–3(i), nondestructive testing of a multilayer integrated circuit using near-IR (1.2 μm) subsurface SI microscopy is shown, where the lateral and axial resolution are of 0.26 and 1.24 μm, respectively;[70] while in Fig. 3(g), we show the electroluminescence emission VIS (700 nm) SI image of a degraded AlGaN/GaN transistor obtained through a SiC substrate with the lateral and axial resolution of 0.3 and 1.7 μm, respectively.[71] Finally, to highlight a potential of SI microscopy in biology and medicine, we show the fluorescence image of transporter protein PH1735 fused with enhanced green fluorescent protein in *Escherichia coli* cells [see Fig. 3(k)] that was obtained via the cryo-compatible (77 K) super SI microscope with strongly subwavelength resolution.[63]

Since the principles of SI microscopy were translated to the THz range,[42–44] this approach has found a number of applications, in particular, in THz biomedicine.[6,15] In Refs. 81 and 84, our group introduced an original arrangement of the THz SI microscope. It uses a backward-wave oscillator, as a source of continuous-wave THz radiation with the output frequency of 0.6 THz (or the wavelength of $\lambda \simeq 500\,\mu$m), and a Golay cell, as a detector of the THz beam power. Figure 4(a) demonstrates the schematic of our SI optical system, which is a crucial element of our THz SI microscope.[81,84] The optical system comprises three elements:

- a rigidly fixed wide-aperture aspherical lens[18] made of high-density polyethylene (HDPE) and featuring the diameter and focal length of 25 and 15 mm, respectively;
- a rigidly fixed hypohemispherical lens made of high-resistivity float-zone silicon (HRFZ-Si) and featuring the diameter and thickness of 10 and 4.65 mm, respectively; its spherical surface is concentric to the convergent wavefront, while its flat surface is perpendicular to the optical axis;
- a movable plane HRFZ-Si window, placed in close contact with the flat surface of HRFZ-Si hemisphere and featuring the diameter and thickness of 50 mm and 250 μm, respectively.

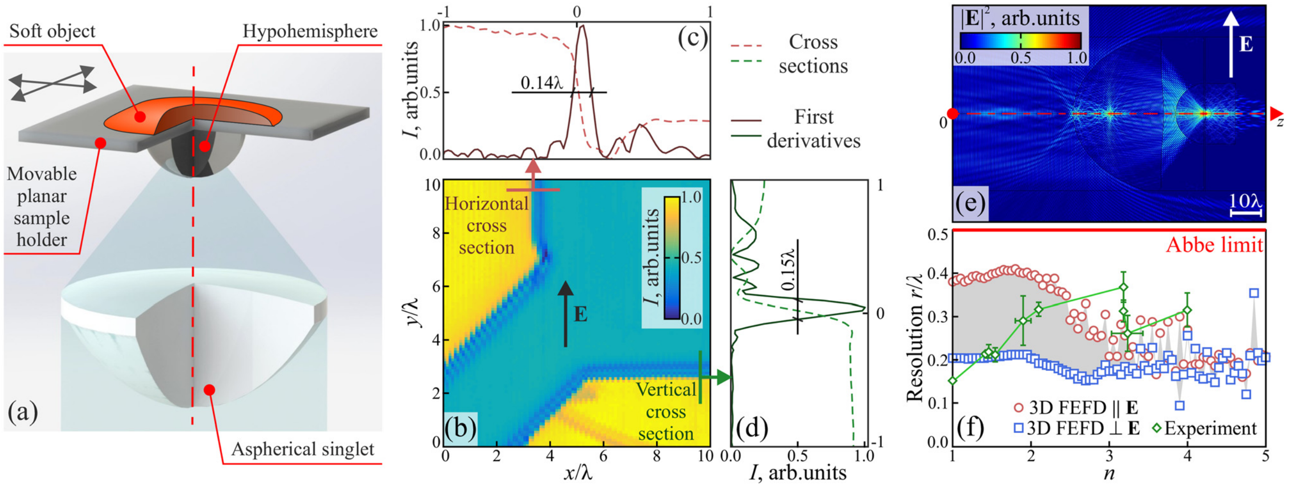

FIG. 4. Composite THz SI lens for imaging of amorphous objects and soft biological tissues *ex vivo*. (a) Schematic of a SI lens comprising a wide-aperture HDPE aspherical singlet, a rigidly fixed HRFZ-Si hypohemisphere, and a movable HRFZ-Si window (sample holder), where the hypohemisphere and window form a unitary hemispherical optical element. (b)–(d) Experimental estimation of the SI lens resolution (in free space—$n_{obj} = 1.0$) based on imaging of a metal test object. Panels (a)–(d) are reproduced with permission from Chernomyrdin *et al.*, Appl. Phys. Lett. **113**, 111102 (2018). Copyright 2018 AIP Publishing. (e) Three-dimensional finite-element frequency-domain (3D-FEFD) modeling of the THz field intensity distribution $I \propto |\mathbf{E}|^2$ in the axial cross section of the SI lens at 0.6 THz, when the imaged object has the refractive index of $n_{obj} = 2$, the absorption coefficient of $\alpha_{obj} = 0$, and the thickness of 10λ. (f) Normalized resolution r/λ of the SI lens estimated as a THz beam spot FWHM as a function of the refractive indices n of a 10λ-thick loss-less ($\alpha_{obj} = 0$) object for two orthogonal polarizations. In (f), the resolution is compared with the experimental estimates from Ref. 82. Panels (e) and (f) are reproduced Chernomyrdin *et al.*, Optica **8**, 1471 (2021). Copyright 2021 The Optical Society.

The system has the maximal aperture angle of $\theta_{max} \simeq 40°$, while HRFZ-Si has the refractive index of $n_{HRFZ-Si} \simeq 3.415$ with negligible chromatic dispersion and absorption in the THz range.

In our THz SI lens, the HRFZ-Si hypohemisphere and window form a unitary optical element—a HRFZ-Si hemispherical SI lens, which serves as a resolution enhancer. At the same time, the HRFZ-Si window is mounted on a motorized translation stage and can be displaced in lateral directions. In this way, such a composite SI lens construction allows imaging of amorphous objects and soft biological tissues *ex vivo*, handled at its shadow side by raster scanning of their surface with a focused THz beam.

Figures 4(b)–4(d) show that our THz SI microscope provides the resolution down to $\geq 0.15\lambda$, when operating with free space at the shadow side of a SI lens. This resolution estimates were obtained experimentally by studying semi-infinite metal test objects with abrupt reflectivity changes, as described in Ref. 81. Also, we reported in Ref. 85 that our system has a small depth of field 0.1–0.2λ and large tolerances ($\sim\lambda$) for the optical elements alignment.

Evidently, resolution of SI microscopy depends on the optical properties of an imaged object, similarly to any other near-field imaging modality. For our THz SI lens, this dependency was studied in Ref. 82. Our numerical and experimental findings revealed that optical properties of an imaged object regulate the TIR conditions at the SI lens–object interface, as well as a contribution of the ordinary and evanescent waves to the beam caustic formation. As shown in Figs. 4(e) and 4(f), the resolution remains strongly sub-wavelength 0.15–0.4λ for the wide range of the object refractive indices $n_{obj} \in (1.0, 5.0)$ and power absorption coefficients $\alpha_{obj} \in (0, 400)$ cm^{-1}. Two regimes of SI microscopy were identified. The first is the TIR regime that appears when the object refractive index is relatively low, and the sub-wavelength resolution is enabled by both ordinary and evanescent waves at the SI lens–object interface. The second is the ordinary reflection regime that occurs when the object refractive index is high enough, so that there is no more TIR effect at the interface, and only the ordinary waves inside a SI lens material are responsible for the SI lens superresolution. Given linear nature of Maxwell's equations, these results are applicable for analysis of SI lenses operating in other spectral ranges.[82]

To demonstrate practical utility of THz SI microscopy, it was applied to study objects of different nature such as electrical circuits and soft biological tissues *ex vivo.*[81,84–86] Particularly, the superresolution THz images of a plant (poinsettia) leaf with subwavelength veins, submillimeter-diameter cell spheroids (made of chondrocytes from the articular hyaline cartilage of male sheep), fibrous connective tissues of the human breast (with embedded separate subwavelength fat cell and mammary gland ducts), muscle tissues of the human tongue (formed by subwavelength longitudinal and transverse muscle fibers), as well as tissues scaffolds (decellularized bovine pericardium collagen matrices) were measured and analyzed. The observed data have revealed strongly subwavelength features of tissues and have confirmed superresolution capabilities of our microscope, as well as its prospects in THz biophotonics.

Despite the widespread use of SI microscopy in the VIS and IR ranges, as well as recent achievements in the THz range, this approach usually results in qualitative images that represent only the raw distributions of the backscattered field intensity over the object surface. Meanwhile, unlocking information about the physical properties of an object, such as its complex refractive index $\tilde{n}_{obj}$, requires resolving the inverse problem of SI microscopy. To address this challenge, in Ref. 83, the quantitative superresolution SI microscopy technique was developed and implemented to the THz frequency range. This method allows reconstruction of the refractive index distribution at the imaging plane with subwavelength resolution, while only the intensity measurements are performed.

At each point of the imaged object surface, this method retrieves its complex refractive index as

$$\tilde{n}_{\mathrm{obj}} = n_{\mathrm{obj}} - i\frac{c_0}{4\pi\nu}\alpha_{\mathrm{obj}}, \tag{3}$$

where $c_0 \simeq 3 \times 10^8$ m/s is the speed of light in free space, and the absorption α_{obj} is defined by power via minimization of the error function, which characterizes discrepancy between the experiment data and analytical model

$$\tilde{n}_{\mathrm{obj}} = \arg\min_{\tilde{n}_{\mathrm{obj}}}\left[\frac{I^{\mathrm{obj}}_{\mathrm{exp}}}{I^{\mathrm{ref}}_{\mathrm{exp}}} - \frac{I_{\mathrm{th}}(\tilde{n}_{\mathrm{obj}})}{I_{\mathrm{th}}(\tilde{n}_{\mathrm{ref}})}\right], \tag{4}$$

where $I^{\mathrm{obj}}_{\mathrm{exp}}$ and $I^{\mathrm{ref}}_{\mathrm{exp}}$ are the experimentally measured sample and reference signals that represent intensities of the electromagnetic fields, which are back-scattered from the SI lens, respectively; $I^{\mathrm{obj}}_{\mathrm{exp}}$ is obtained for an imaged object, while $I^{\mathrm{ref}}_{\mathrm{exp}}$ is for a reference medium with known complex refractive index $\tilde{n}_{\mathrm{ref}}$. In Ref. 83, we use air as such a reference medium ($\tilde{n}_{\mathrm{ref}} = 1.0$), while other options are also available. The sample signal $I^{\mathrm{obj}}_{\mathrm{exp}}$ is normalized by a reference one $I^{\mathrm{ref}}_{\mathrm{exp}}$ to filter out a contribution of the Si microscope response function.

In Eq. (4), the function $I_{\mathrm{th}}(\tilde{n}_{\mathrm{obj}})$ stands for a model of the back-scattered field intensity, which can be either defined analytically or computed numerically for a SI lens with an imaged object at its shadow side that has a form of a thick ($\gg \lambda$) slab with the complex refractive index $\tilde{n}_{\mathrm{obj}}$. This model should incorporate all the key features of the electromagnetic-wave interaction with the SI lens and an object: contributions of the ordinary and evanescent waves, wide beam aperture, light polarization and coherence length, standing waves inside a SI lens, etc. Thanks to a quite simple geometry of our THz SI lens, in Ref. 83, the fully analytical model was derived, which was then proved via full-vector numerical analysis.

Since it is impossible to estimate two variables n_{obj} and α_{obj} relying only on a single measured intensity value I_{exp}, some physical relation between n_{obj} and α_{obj} should be defined, thus, restricting the developed method generality. For this purpose, in Ref. 83, a particular case of the developed method operation is considered—i.e., THz microscopy of hydrated biological tissues, the effective THz dielectric response of which is commonly interpreted within the effective medium theory and determined completely by the content of tissue water,[87] while the latter also plays a role of main endogenous label of pathological processes.[6,15,17] In this way, THz dielectric response of tissues can be modeled based on that of bulk water $\tilde{n}_{\mathrm{H2O}}$, dehydrated tissues $\tilde{n}_{\mathrm{dry}}$, and the tissue water content C using, for example, the Bruggeman effective medium model

$$\frac{\tilde{n}^2_{\mathrm{H2O}} - \tilde{n}^2_{\mathrm{obj}}(C)}{\tilde{n}^2_{\mathrm{H2O}} + 2\tilde{n}^2_{\mathrm{obj}}(C)}C + \frac{\tilde{n}^2_{\mathrm{dry}} - \tilde{n}^2_{\mathrm{obj}}(C)}{\tilde{n}^2_{\mathrm{dry}} + 2\tilde{n}^2_{\mathrm{obj}}(C)}(1 - C) = 0. \tag{5}$$

Thus, Eqs. (4) and (5) yield quite accurate predictions for both the complex refractive index $\tilde{n}_{\mathrm{obj}}$ and water content C in tissues.[83]

The developed quantitative superresolution THz SI microscope was used to study *ex vivo* the freshly excised (hydrated) intact brain tissues and glioma model 101.8 from rats.[83,88] The THz neurodiagnosis of brain tumors attracts considerable attention thanks to the label-free character of contrast between intact tissues and tumors, which was reported for both glioma models from animals and human brain gliomas *ex vivo*.[89] The refractive index n_{obj} and absorption coefficient α_{obj} distributions, as well as the tissue water content C, observed in the THz data from Fig. 5, overall agree with the previous studies involving different diffraction-limited THz spectrometers and imaging systems.[89] Thus, as compared to other experimental techniques, quantitative THz SI microscopy provides reasonable estimates of higher refractive indices, absorption coefficient, and water content in a tumor as compared to the intact tissues. Additionally, superior resolution of our THz SI microscope revealed considerable heterogeneity of the brain tissues at scale posed by the THz wavelengths. From Fig. 5, we notice a pronounced difference between the THz response of the white matter and gray matter (cortex), as well as the tumor heterogeneity that can be attributed to a number of factors such as the tumor cells' accumulations, vessels, hemorrhages, and necrotic debris.

Our findings highlighted that THz SI microscopy has few important advantages over the existing modalities of THz spectroscopy and imaging. Among them are its superior resolution, high energy efficiency, and an ability to extract quantitative information about an object such as distributions of its complex refractive index $\tilde{n}_{\mathrm{obj}}$, water content C (in hydrated media), or other physical quantities. In our opinion, these advantages allow the developed technique to be used in a number of demanding fields in material sciences, nondestructive testing, chemistry, pharmaceutical industry, and biomedicine. Particularly, it can be used to study the Mie scattering of THz waves and the THz-wave transport in heterogeneous objects[54] or in medical diagnosis of malignant and benign neoplasms with different nosologies and localizations.[15]

At the same time, we can point out several ways to further improve the THz SI microscopy performance and, thus, to extend its considerable practical utility. The resolution of our imaging system can be further enhanced by substituting the HRFZ-Si with another THz optical material for SI lens fabrication that has higher THz refractive index along with an appropriate THz-wave absorption. As candidates, bulk sapphire (α-Al_2O_3)[34] and rutile (TiO_2)[90] crystals, TiO_2 nanoparticle-based composites,[91] PbTe and GeTe,[92] or high-refractive-index metamaterials[53] can be mentioned. We should stress that many high-refractive-index crystalline optical materials, such as sapphire or rutile, possess considerable optical anisotropy. Effects of crystal anisotropy and orientation, as well as electromagnetic-beam polarization on the SI microscopy performance should be carefully studied when designing such crystalline SI lenses.

The THz SI microscope performance is strongly limited by the duration of image acquisition, which is due to inertness of a scanning system and a Golay cell. To considerably boost the THz SI microscope performance, one can imply multipixel detectors[93] and fast rotary delay stages.[94] THz SI microscopy can be generalized for direct imaging of the complex (absorbing) media using the field amplitude detectors such as THz photoconductive antennas.[1,4] Indeed, by detecting and analyzing both the intensity and phase of the backscattered field in a SI microscope, it is possible to unambiguously estimate the refractive index n_{obj} and absorption coefficient α_{obj} of an imaged object without any physical assumptions on the object material properties. It is also worth noting that the developed SI lens reflectivity model[83]

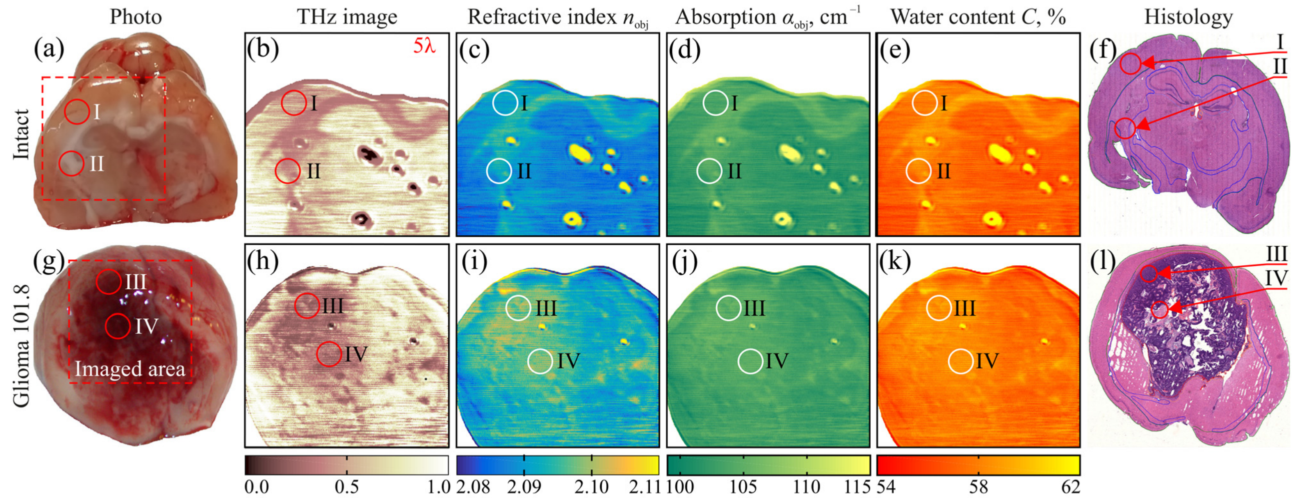

FIG. 5. Quantitative THz SI microscopy at $\nu = 0.6$ THz ($\lambda \simeq 500\ \mu$m) of the *ex vivo* freshly excised intact brain and glioma model 101.8 from rats. (a)–(f) Visible photo, THz image, refractive index n_{obj}, power absorption coefficient α_{obj}, and water content C distributions, as well as hematoxylin and eosin-stained histology, respectively, for the intact rat brain. Here, markers I and II point the gray matter (cortex) and white matter, respectively. (g)–(l) Similar data set for a tumor, where markers III and IV indicate the accumulation of tumor cells and the necrotic debris. Adapted with the permission from Chernomyrdin *et al.*, Optica **8**, 1471 (2021). Copyright 2021 The Optical Society.

can be easily generalized to interpret such complex signals in different spectral ranges.

Various electro- and magneto-dipole excitations of matter can underlie the linear and nonlinear electrodynamic response of an object in different spectral ranges, while only linear complex dielectric permittivity (or complex refractive index) can be studied using the discussed quantitative SI microscopy method.[83,86,88] Thus, this method is still to be adapted for studying the magnetic permeability and non-linear electrodynamic characteristics of a sample. The resultant method has a potential not only in biophotonics but also in other branches of fundamental and applied physics, including condensed matter physics, magnetism, nonlinear optics, and semiconductor electronics.

Despite the object-dependent character of a SI lens was reported in Ref. 82, the THz beam focusing in such systems can be also affected by heterogeneous character and scattering properties of an object. The investigation of such effects as well as the development of approaches for mitigating them (for example, modern method of immersion optical clearing[95]) can be considered as a promising topic for the further research in the field of THz SI microscopy.

SI microscopy should not be confused with other imaging modalities that also rely on the TIR and near-field phenomena. Among them, we first consider microscopy with the TIR excitation of a sample,[96–98] which provides high contrast between a sample and a substrate (a TIR prism), offers a variety of applications in biology and medicine, but still obeys the Abbe barrier. We also notice that SI microscopy differs from dielectric microparticle-assisted microscopy.[99,100] The latter relies on the aforementioned photonic jet effect or the whispering gallery modes, which yield strong electromagnetic-wave confinement at the shadow side of a mesoscale ($\sim\lambda$) dielectric particle and result in a slightly subwavelength resolution of $\sim 10^{-1}\lambda$.[23,101–103] Such imaging principles were vigorously explored in the VIS and IR ranges and then translated to the THz band.[24,25,104] However, they still suffer from a problem of small dielectric particle handling in front of focal plane during imaging. Finally, in Ref. 105, it was theoretically predicted that a favorable combination of the SI and photonic jet effects in a single high-refractive-index dielectric particle can boost the THz microscopy performance, but this concept is still to be verified experimentally.

In conclusion, in this paper, we have considered principles of SI microscopy, its technical realizations, and applications in the VIS and IR ranges, as well as its recent translation to the THz band. We showed that this THz imaging modality offers a compromise between the superior resolution and high energy efficiency. Moreover, we demonstrated that SI microscopy can be easily applied for solving the emerging problems of different branches of THz science and technology. We also discussed recent achievements and challenging problems of THz SI microscopy.

Experimental study by N. V. Chernomyrdin, V. V. Bukin, and K. I. Zaytsev was supported by the Ministry of Science and Higher Education of the Russian Federation, Project No. 075-15-2020-790. Numerical simulation by M. Skorobogatiy was supported by the Ubiquitous Terahertz Photonics Project within the Canada Research Chairs Program.

AUTHOR DECLARATIONS

Conflict of Interest

The authors have no conflicts to disclose.

DATA AVAILABILITY

The data that support the findings of this study are available from the corresponding author upon reasonable request.

REFERENCES

[1]S. Lepeshov, A. Gorodetsky, A. Krasnok, E. Rafailov, and P. Belov, "Enhancement of terahertz photoconductive antenna operation by optical nanoantennas," Laser Photonics Rev. **11**, 1600199 (2017).

[2] H. Guerboukha, K. Nallappan, and M. Skorobogatiy, "Toward real-time terahertz imaging," Adv. Opt. Photonics **10**, 843–938 (2018).
[3] V. Ryzhii, T. Otsuji, and M. Shur, "Graphene based plasma-wave devices for terahertz applications," Appl. Phys. Lett. **116**, 140501 (2020).
[4] A. Yachmenev, S. Pushkarev, R. Reznik, R. Khabibullin, and D. Ponomarev, "Arsenides-and related III–V materials-based multilayered structures for terahertz applications: Various designs and growth technology," Prog. Cryst. Growth Charact. Mater. **66**, 100485 (2020).
[5] M. Islam, C. Cordeiro, M. Franco, J. Sultana, A. Cruz, and D. Abbott, "Terahertz optical fibers," Opt. Express **28**, 16089–16117 (2020).
[6] O. Smolyanskaya, N. Chernomyrdin, A. Konovko, K. Zaytsev, I. Ozheredov, O. Cherkasova, M. Nazarov, J.-P. Guillet, S. Kozlov, Y. Kistenev, J.-L. Coutaz, P. Mounaix, V. Vaks, J.-H. Son, H. Cheon, V. Wallace, Y. Feldman, I. Popov, A. Yaroslavsky, A. Shkurinov, and V. Tuchin, "Terahertz biophotonics as a tool for studies of dielectric and spectral properties of biological tissues and liquids," Prog. Quantum Electron. **62**, 1–77 (2018).
[7] B. Giuliano, A. Gavdush, B. Muller, K. Zaytsev, T. Grassi, A. Ivlev, M. Palumbo, G. Baratta, C. Scire, G. Komandin, S. Yurchenko, and P. Caselli, "Broadband spectroscopy of astrophysical ice analogues—I. Direct measurement of the complex refractive index of CO ice using terahertz time-domain spectroscopy," Astron. Astrophys. **629**, A112 (2019).
[8] N. Wang, S. Cakmakyapan, Y.-J. Lin, H. Javadi, and M. Jarrahi, "Room-temperature heterodyne terahertz detection with quantum-level sensitivity," Nat. Astron. **3**, 977–982 (2019).
[9] H. Hafez, S. Kovalev, K.-J. Tielrooij, M. Bonn, M. Gensch, and D. Turchinovich, "Terahertz nonlinear optics of graphene: From saturable absorption to high-harmonics generation," Adv. Opt. Mater. **8**, 1900771 (2020).
[10] M. Burdanova, A. Tsapenko, M. Kharlamova, E. Kauppinen, B. Gorshunov, J. Kono, and J. Lloyd-Hughes, "A review of the terahertz conductivity and photoconductivity of carbon nanotubes and heteronanotubes," Adv. Opt. Mater. **9**, 2101042 (2021).
[11] J. Zeitler, P. Taday, D. Newnham, M. Pepper, K. Gordon, and T. Rades, "Terahertz pulsed spectroscopy and imaging in the pharmaceutical setting—A review," J. Pharm. Pharmacol. **59**, 209–223 (2010).
[12] A. Ren, A. Zahid, D. Fan, X. Yang, M. Imran, A. Alomainy, and Q. Abbasi, "State-of-the-art in terahertz sensing for food and water security—A comprehensive review," Trends Food Sci. Technol. **85**, 241–251 (2019).
[13] J. True, C. Xi, N. Jessurun, K. Ahi, and N. Asadizanjani, "Review of THz-based semiconductor assurance," Opt. Eng. **60**, 060901 (2021).
[14] N. Yardimci, H. Lu, and M. Jarrahi, "High power telecommunication-compatible photoconductive terahertz emitters based on plasmonic nanoantenna arrays," Appl. Phys. Lett. **109**, 191103 (2016).
[15] K. Zaytsev, I. Dolganova, N. Chernomyrdin, G. Katyba, A. Gavdush, O. Cherkasova, G. Komandin, M. Shchedrina, A. Khodan, D. Ponomarev, I. Reshetov, V. Karasik, M. Skorobogatiy, V. Kurlov, and V. Tuchin, "The progress and perspectives of terahertz technology for diagnosis of neoplasms: A review," J. Opt. **22**, 013001 (2020).
[16] H. Lindley-Hatcher, R. Stantchev, X. Chen, A. Hernandez-Serrano, J. Hardwicke, and E. Pickwell-MacPherson, "Real time THz imaging—opportunities and challenges for skin cancer detection," Appl. Phys. Lett. **118**, 230501 (2021).
[17] O. Cherkasova, D. Serdyukov, E. Nemova, A. Ratushnyak, A. Kucheryavenko, I. Dolganova, G. Xu, M. Skorobogatiy, I. Reshetov, P. Timashev, I. Spektor, K. Zaytsev, and V. Tuchin, "Cellular effects of terahertz waves," J. Biomed. Opt. **26**, 090902 (2021).
[18] N. Chernomyrdin, M. Frolov, S. Lebedev, I. Reshetov, I. Spektor, V. Tolstoguzov, V. Karasik, A. Khorokhorov, K. Koshelev, A. Schadko, S. Yurchenko, and K. Zaytsev, "Wide-aperture aspherical lens for high-resolution terahertz imaging," Rev. Sci. Instrum. **88**, 014703 (2017).
[19] K. Ahi, "Mathematical modeling of THz point spread function and simulation of THz imaging systems," IEEE Trans. Terahertz Sci. Technol. **7**, 747–754 (2017).
[20] K. McClatchey, M. Reiten, and R. Cheville, "Time resolved synthetic aperture terahertz impulse imaging," Appl. Phys. Lett. **79**, 4485–4487 (2001).
[21] H. Guerboukha, K. Nallappan, and M. Skorobogatiy, "Exploiting k-space/frequency duality toward real-time terahertz imaging," Optica **5**, 109–116 (2018).
[22] N. Petrov, J.-B. Perraud, A. Chopard, J.-P. Guillet, O. Smolyanskaya, and P. Mounaix, "Terahertz phase retrieval imaging in reflection," Opt. Lett. **45**, 4168–4171 (2020).
[23] L. Yue, O. Minin, Z. Wang, J. Monks, A. Shalin, and I. Minin, "Photonic hook: A new curved light beam," Opt. Lett. **43**, 771–774 (2018).
[24] H. Pham, S. Hisatake, O. Minin, T. Nagatsuma, I. Minin, H. Pham, N. Huy, S. Hisatake, O. Minin, T. Nagatsuma, and I. Minin, "Enhancement of spatial resolution of terahertz imaging systems based on terajet generation by dielectric cube," APL Photonics **2**, 056106 (2017).
[25] I. Minin, O. Minin, G. Katyba, N. Chernomyrdin, V. Kurlov, K. Zaytsev, L. Yue, Z. Wang, and D. Christodoulides, "Experimental observation of a photonic hook," Appl. Phys. Lett. **114**, 031105 (2019).
[26] N. van der Valk and P. Planken, "Electro-optic detection of subwavelength terahertz spot sizes in the near field of a metal tip," Appl. Phys. Lett. **81**, 1558–1560 (2002).
[27] H.-T. Chen, R. Kersting, and G. Cho, "Terahertz imaging with nanometer resolution," Appl. Phys. Lett. **83**, 3009–3011 (2003).
[28] A. Huber, F. Keilmann, J. Wittborn, J. Aizpurua, and R. Hillenbrand, "Terahertz near-field nanoscopy of mobile carriers in single semiconductor nanodevices," Nano Lett. **8**, 3766–3770 (2008).
[29] J. Buron, D. Petersen, P. Boggild, D. Cooke, M. Hilke, J. Sun, E. Whiteway, P. Nielsen, O. Hansen, A. Yurgens, and P. Jepsen, "Graphene conductance uniformity mapping," Nano Lett. **12**, 5074–5081 (2012).
[30] M. Awad, M. Nagel, and H. Kurz, "Tapered sommerfeld wire terahertz near-field imaging," Appl. Phys. Lett. **94**, 051107 (2009).
[31] C. R. Simovski, P. A. Belov, A. V. Atrashchenko, and Y. S. Kivshar, "Wire metamaterials: Physics and applications," Adv. Mater. **24**, 4229–4248 (2012).
[32] M. Habib, A. Stefani, S. Atakaramians, S. Fleming, A. Argyros, and B. Kuhlmey, "A prism based magnifying hyperlens with broad-band imaging," Appl. Phys. Lett. **110**, 101106 (2017).
[33] G. Katyba, D. Melikyants, N. Chernomyrdin, V. Kurlov, and K. Zaytsev, "Terahertz transmission-mode scanning-probe near-field optical microscopy based on a flexible step-index sapphire fiber," Opt. Eng. **60**, 082010 (2021).
[34] K. Zaytsev, G. Katyba, N. Chernomyrdin, I. Dolganova, A. Kucheryavenko, A. Rossolenko, V. Tuchin, V. Kurlov, and M. Skorobogatiy, "Overcoming the Abbe diffraction limit using a bundle of metal-coated high-refractive-index sapphire optical fibers," Adv. Opt. Mater. **8**, 2000307 (2020).
[35] U. Schade, K. Holldack, P. Kuske, G. Wüstefeld, and H.-W. Hübers, "THz near-field imaging employing synchrotron radiation," Appl. Phys. Lett. **84**, 1422–1424 (2004).
[36] K. Ishihara, K. Ohashi, T. Ikari, H. Minamide, H. Yokoyama, J-i. Shikata, and H. Ito, "Terahertz-wave near-field imaging with subwavelength resolution using surface-wave-assisted bow-tie aperture," Appl. Phys. Lett. **89**, 201120 (2006).
[37] A. Macfaden, J. Reno, I. Brener, and O. Mitrofanov, "3 μm aperture probes for near-field terahertz transmission microscopy," Appl. Phys. Lett. **104**, 011110 (2014).
[38] R. Stantchev, B. Sun, S. Hornett, P. Hobson, G. Gibson, M. Padgett, and E. Hendry, "Noninvasive, near-field terahertz imaging of hidden objects using a single-pixel detector," Sci. Adv. **2**, e1600190 (2016).
[39] S. Kim, H. Murakami, and M. Tonouchi, "Transmission-type laser THz emission microscope using a solid immersion lens," IEEE J. Sel. Top. Quantum Electron. **14**, 498–504 (2008).
[40] K. Okada, K. Serita, Z. Zang, H. Murakami, I. Kawayama, Q. Cassar, G. Macgrogan, J.-P. Guillet, P. Mounaix, and M. Tonouchi, "Scanning laser terahertz near-field reflection imaging system," Appl. Phys. Express **12**, 122005 (2019).
[41] S. M. Mansfield and G. S. Kino, "Solid immersion microscope," Appl. Phys. Lett. **57**, 2615–2616 (1990).
[42] A. Pimenov and A. Loidl, "Focusing of millimeter-wave radiation beyond the Abbe barrier," Appl. Phys. Lett. **83**, 4122–4124 (2003).
[43] B. Gompf, M. Gerull, T. Muller, and M. Dressel, "THz-micro-spectroscopy with backward-wave oscillators," Infrared Phys. Technol. **49**, 128–132 (2006).
[44] N. Chernomyrdin, A. Schadko, S. Lebedev, V. Tolstoguzov, V. Kurlov, I. Reshetov, I. Spektor, M. Skorobogatiy, S. Yurchenko, and K. Zaytsev, "Solid immersion terahertz imaging with sub-wavelength resolution," Appl. Phys. Lett. **110**, 221109 (2017).

[45]T. Milster, J. Jo, and K. Hirota, "Roles of propagating and evanescent waves in solid immersion lens systems," Appl. Opt. **38**, 5046–5057 (1999).
[46]K. Serrels, E. Ramsay, P. Dalgarno, B. Gerardot, J. O'Connor, R. Hadfield, R. Warburton, and D. Reid, "Solid immersion lens applications for nanophotonic devices," J. Nanophotonics **2**, 021854 (2008).
[47]R. Brunner, M. Ferstl, S. Hohng, J. White, M. Burkhardt, A. Pesch, and O. Sandfuchs, "Diffraction-based solid immersion lens," J. Opt. Soc. Am. A **21**, 1186 (2004).
[48]H. Moon, Y.-J. Yoon, W.-C. Kim, N.-C. Park, K.-S. Park, and Y.-P. Park, "A study on the realization of high resolution solid immersion lens-based near-field imaging optics by use of an annular aperture," Opt. Express **18**, 17533 (2010).
[49]C. Liu and S.-H. Park, "Numerical analysis of an annular-aperture solid immersion lens," Opt. Lett. **29**, 1742–1744 (2004).
[50]D. Fletcher, K. Crozier, C. Quate, G. Kino, K. Goodson, D. Simanovskii, and D. Palanker, "Near-field infrared imaging with a microfabricated solid immersion lens," Appl. Phys. Lett. **77**, 2109–2111 (2000).
[51]G. Lerman, A. Israel, and A. Lewis, "Applying solid immersion near-field optics to Raman analysis of strained silicon thin films," Appl. Phys. Lett. **89**, 223122 (2006).
[52]W. Challener, C. Mihalcea, C. Peng, and K. Pelhos, "Miniature planar solid immersion mirror with focused spot less than a quarter wavelength," Opt. Express **13**, 7189–7197 (2005).
[53]W. Fan, B. Yan, Z. Wang, and L. Wu, "Three-dimensional all-dielectric metamaterial solid immersion lens for subwavelength imaging at visible frequencies," Sci. Adv. **2**, 40–42 (2016).
[54]A. Ishimaru, *Electromagnetic Wave Propagation, Radiation, and Scattering: From Fundamentals to Applications*, 2nd ed. (Wiley—IEEE Press, Hoboken, New Jersey, 2017), p. 968.
[55]M. Born and E. Wolf, *Principles of Optics*, 6th ed. (Pergamon, USA, 1980).
[56]M. Baba, T. Sasaki, M. Yoshita, and H. Akiyama, "Aberrations and allowances for errors in a hemisphere solid immersion lens for submicron-resolution photoluminescence microscopy," J. Appl. Phys. **85**, 6923–6925 (1999).
[57]K. Karrai, X. Lorenz, and L. Novotny, "Enhanced reflectivity contrast in confocal solid immersion lens microscopy," Appl. Phys. Lett. **77**, 3459–3461 (2000).
[58]L. Helseth, "Roles of polarization, phase and amplitude in solid immersion lens systems," Opt. Commun. **191**, 161–172 (2001).
[59]S. Ippolito, B. Goldberg, and M. Unlu, "Theoretical analysis of numerical aperture increasing lens microscopy," J. Appl. Phys. **97**, 053105 (2005).
[60]W.-C. Kim, Y.-J. Yoon, H. Choi, N.-C. Park, and Y.-P. Park, "Effects of optical variables in immersion lens-based near-field optics," Opt. Express **16**, 13933–13948 (2008).
[61]Y.-J. Yoon, W.-C. Kim, N.-C. Park, K.-S. Park, and Y.-P. Park, "Feasibility study of the application of radially polarized illumination to solid immersion lens-based near-field optics," Opt. Lett. **34**, 1961–1963 (2009).
[62]K. Huang and Y. Li, "Realization of a subwavelength focused spot without a longitudinal field component in a solid immersion lens-based system," Opt. Lett. **36**, 3536 (2011).
[63]L. Wang, B. Bateman, L. Zanetti-Domingues, A. Moores, S. Astbury, C. Spindloe, M. Darrow, M. Romano, S. Needham, K. Beis, D. Rolfe, D. Clarke, and M. Martin-Fernandez, "Solid immersion microscopy images cells under cryogenic conditions with 12 nm resolution," Commun. Biol. **2**, 74 (2019).
[64]S. Ippolito, P. Song, D. Miles, and J. Sylvestri, "Angular spectrum tailoring in solid immersion microscopy for circuit analysis," Appl. Phys. Lett. **92**, 101109 (2008).
[65]L. P. Ghislain, V. B. Elings, K. B. Crozier, S. R. Manalis, S. C. Minne, K. Wilder, G. S. Kino, and C. F. Quate, "Near-field photolithography with a solid immersion lens," Appl. Phys. Lett. **74**, 501–503 (1999).
[66]G. Tessier, M. Bardoux, C. Boue, C. Filloy, and D. Fournier, "Back side thermal imaging of integrated circuits at high spatial resolution," Appl. Phys. Lett. **90**, 171112 (2007).
[67]C. Peng, C. Mihalcea, D. Buchel, W. Challener, and E. Gage, "Near-field optical recording using a planar solid immersion mirror," Appl. Phys. Lett. **87**, 151105 (2005).
[68]Z. Liu, B. Goldberg, S. Ippolito, A. Vamivakas, M. Unlu, and R. Mirin, "High resolution, high collection efficiency in numerical aperture increasing lens microscopy of individual quantum dots," Appl. Phys. Lett. **87**, 071905 (2005).
[69]C. Michaels, "Surface-sensitive Raman microscopy with total internal reflection illumination," J. Raman Spectrosc. **41**, 1670–1677 (2010).
[70]F. Koklu, J. Quesnel, A. Vamivakas, S. Ippolito, B. Goldberg, and M. Unlu, "Widefield subsurface microscopy of integrated circuits," Opt. Express **16**, 9501 (2008).
[71]J. Pomeroy and M. Kuball, "Solid immersion lenses for enhancing the optical resolution of thermal and electroluminescence mapping of GaN-on-SiC transistors," J. Appl. Phys. **118**, 144501 (2015).
[72]W.-S. Lee, T. Kim, G.-J. Choi, G. Lim, H.-E. Joe, M.-G. Gang, H. Moon, D.-H. Kim, B.-K. Min, Y.-P. Park, and N.-C. Park, "Experimental demonstration of line-width modulation in plasmonic lithography using a solid immersion lens-based active nano-gap control," Appl. Phys. Lett. **106**, 051111 (2015).
[73]S. Ippolito, S. Thorne, M. Eraslan, B. Goldberg, M. Unlu, and Y. Leblebici, "High spatial resolution subsurface thermal emission microscopy," Appl. Phys. Lett. **84**, 4529–4531 (2004).
[74]B. Terris, H. Mamin, D. Rugar, W. Studenmund, and G. Kino, "Near-field optical data storage using a solid immersion lens," Appl. Phys. Lett. **65**, 388–390 (1994).
[75]B. Terris, H. Mamin, and D. Rugar, "Near-field optical data storage," Appl. Phys. Lett. **68**, 141–143 (1996).
[76]A. Madrazo and M. Nieto-Vesperinas, "Model near field calculations for optical data storage readout," Appl. Phys. Lett. **70**, 31–33 (1997).
[77]C. Poweleit, A. Gunther, S. Goodnick, and J. Menendez, "Raman imaging of patterned silicon using a solid immersion lens," Appl. Phys. Lett. **73**, 2275–2277 (1998).
[78]Q. Wu, R. Grober, D. Gammon, and D. Katzer, "Imaging spectroscopy of two-dimensional excitons in a narrow GaAs/AlGaAs quantum well," Phys. Rev. Lett. **83**, 2652–2655 (1999).
[79]R. Hadfield, P. Dalgarno, J. O'Connor, E. Ramsay, R. Warburton, E. Gansen, B. Baek, M. Stevens, R. Mirin, and S. Nam, "Submicrometer photoresponse mapping of nanowire superconducting single-photon detectors," Appl. Phys. Lett. **91**, 241108 (2007).
[80]A. Vamivakas, M. Atatüre, J. Dreiser, S. Yilmaz, A. Badolato, A. Swan, B. Goldberg, A. Imamğlu, and M. Unlu, "Strong extinction of a far-field laser beam by a single quantum dot," Nano Lett. **7**, 2892–2896 (2007).
[81]N. Chernomyrdin, A. Kucheryavenko, G. Kolontaeva, G. Katyba, I. Dolganova, P. Karalkin, D. Ponomarev, V. Kurlov, I. Reshetov, M. Skorobogatiy, V. Tuchin, and K. Zaytsev, "Reflection-mode continuous-wave 0.15λ-resolution terahertz solid immersion microscopy of soft biological tissues," Appl. Phys. Lett. **113**, 111102 (2018).
[82]V. Zhelnov, K. Zaytsev, A. Kucheryavenko, G. Katyba, I. Dolganova, D. Ponomarev, V. Kurlov, M. Skorobogatiy, and N. Chernomyrdin, "Object-dependent spatial resolution of the reflection-mode terahertz solid immersion microscopy," Opt. Express **29**, 3553 (2021).
[83]N. Chernomyrdin, M. Skorobogatiy, A. Gavdush, G. Musina, G. Katyba, G. Komandin, A. Khorokhorov, I. Spektor, V. Tuchin, and K. Zaytsev, "Quantitative super-resolution solid immersion microscopy via refractive index profile reconstruction," Optica **8**, 1471 (2021).
[84]N. Chernomyrdin, A. Kucheryavenko, E. Rimskaya, I. Dolganova, V. Zhelnov, P. Karalkin, A. Gryadunova, I. Reshetov, D. Lavrukhin, D. Ponomarev, V. Karasik, and K. Zaytsev, "Terahertz microscope based on solid immersion effect for imaging of biological tissues," Opt. Spectrosc. **126**, 560–567 (2019).
[85]N. Chernomyrdin, V. Zhelnov, A. Kucheryavenko, I. Dolganova, G. Katyba, V. Karasik, I. Reshetov, and K. Zaytsev, "Numerical analysis and experimental study of terahertz solid immersion microscopy," Opt. Eng. **59**, 061605 (2019).
[86]G. Musina, N. Chernomyrdin, E. Gafarova, A. Gavdush, A. Shpichka, G. Komandin, V. Anzin, E. Grebenik, M. Kravchik, E. Istranova, I. Dolganova, K. Zaytsev, and P. Timashev, "Moisture adsorption by decellularized bovine pericardium collagen matrices studied by terahertz pulsed spectroscopy and solid immersion microscopy," Biomed. Opt. Express **12**, 5368–5386 (2021).
[87]S. Yamaguchi, Y. Fukushi, O. Kubota, T. Itsuji, T. Ouchi, and S. Yamamoto, "Origin and quantification of differences between normal and tumor tissues observed by terahertz spectroscopy," Phys. Med. Biol. **61**, 6808–6820 (2016).
[88]A. Kucheryavenko, N. Chernomyrdin, A. Gavdush, A. Alekseeva, P. Nikitin, I. Dolganova, P. Karalkin, A. Khalansky, I. Spektor, M. Skorobogatiy, V. Tuchin, and K. Zaytsev, "Terahertz dielectric spectroscopy and solid

immersion microscopy of *ex vivo* glioma model 101.8: Brain tissue heterogeneity," Biomed. Opt. Express **12**, 5272–5289 (2021).
[89]G. Musina, P. Nikitin, N. Chernomyrdin, I. Dolganova, A. Gavdush, G. Komandin, D. Ponomarev, A. Potapov, I. Reshetov, V. Tuchin, and K. Zaytsev, "Prospects of terahertz technology in diagnosis of human brain tumors—A review," J. Biomed. Photonics Eng. **6**, 020201 (2020).
[90]K. Berdel, J. Rivas, P. Bolivar, P. de Maagt, and H. Kurz, "Temperature dependence of the permittivity and loss tangent of high-permittivity materials at terahertz frequencies," IEEE Trans. Microwave Theory Tech. **53**, 1266–1271 (2005).
[91]B. Ung, A. Dupuis, K. Stoeffler, C. Dubois, and M. Skorobogatiy, "High-refractive-index composite materials for terahertz waveguides: Trade-off between index contrast and absorption loss," J. Opt. Soc. Am. B **28**, 917–921 (2011).
[92]D. Baranov, D. Zuev, S. Lepeshov, O. Kotov, A. Krasnok, A. Evlyukhin, and B. Chichkov, "All-dielectric nanophotonics: The quest for better materials and fabrication techniques," Optica **4**, 814–825 (2017).
[93]R. Henri, K. Nallappan, D. Ponomarev, H. Guerboukha, D. Lavrukhin, A. Yachmenev, R. Khabibullin, and M. Skorobogatiy, "Fabrication and characterization of an 8×8 terahertz photoconductive antenna array for spatially resolved time domain spectroscopy and imaging applications," IEEE Access **9**, 117691–117702 (2021).
[94]H. Guerboukha, A. Markov, H. Qu, and M. Skorobogatiy, "Time resolved dynamic measurements at THz frequencies using a rotary optical delay line," IEEE Trans. Terahertz Sci. Technol. **5**, 564–572 (2015).
[95]V. Tuchin, D. Zhu, and E. Genina, *Handbook of Tissue Optical Clearing. New Prospects in Optical Imaging*, 1st ed. (CRC Press, 2022), p. 682.
[96]E. Ambrose, "A surface contact microscope for the study of cell movements," Nature **178**, 1194 (1956).
[97]D. Axelrod, "Cell-substrate contacts illuminated by total internal reflection fluorescence," J. Cell Biol. **89**, 141–145 (1981).
[98]C. Sonnichsen, S. Geier, N. Hecker, G. von Plessen, J. Feldmann, H. Ditlbacher, B. Lamprecht, J. Krenn, F. Aussenegg, V.-H. Chan, J. Spatz, and M. Muller, "Spectroscopy of single metallic nanoparticles using total internal reflection microscopy," Appl. Phys. Lett. **77**, 2949–2951 (2000).
[99]S. Lecler, S. Perrin, A. Leong-Hoi, and P. Montgomery, "Photonic jet lens," Sci. Rep. **9**, 4725 (2019).
[100]S. Perrin, Y. Donie, P. Montgomery, G. Gomard, and S. Lecler, "Compensated microsphere-assisted interference microscopy," Phys. Rev. Appl. **13**, 014068 (2020).
[101]B. Luk'yanchuk, R. Paniagua-Dominguez, I. Minin, O. Minin, and Z. Wang, "Refractive index less than two: Photonic nanojets yesterday, today and tomorrow," Opt. Mater. Express **7**, 1820–1847 (2017).
[102]J. Lopes, M. Andrade, J. Leao-Neto, J. Adamowski, I. Minin, and G. Silva, "Focusing acoustic beams with a ball-shaped lens beyond the diffraction limit," Phys. Rev. Appl. **8**, 024013 (2017).
[103]S. Perrin, P. Montgomery, and S. Lecler, "Super-resolution imaging within reach," Opt. Eng. **58**, 050501 (2019).
[104]I. Dorofeev, V. Suslyaev, O. Minin, and I. Minin, "Role of the tangential electric field component to the terahertz jet and hook formation by dielectric cube and sphere," Opt. Eng. **60**, 082004 (2020).
[105]L. Yue, B. Yan, J. Monks, R. Dhama, Z. Wang, O. Minin, and I. Minin, "A millimetre-wave cuboid solid immersion lens with intensity-enhanced amplitude mask apodization," J. Infrared, Millimeter, Terahertz Waves **39**, 546–552 (2018).